Supporting Information

Qu *et al.* 10.1073/pnas.0801436105

SI Materials and Methods

Sample Preparation. Fig. S1 shows the secondary structure of the mutated catalytic domain of thermophilic RNase P RNA from *Bacillus stearothermophilus* (1), termed CthermoL18. To allow FRET measurements, the RNA was mutated for attachment of the Cy3/Cy5 FRET dye pair (2, 3). The 3′ end was extended with 21 nucleotides (shown in blue) to allow hybridization of the complementary DNA oligo, Tether-Cy5 (sequence: 5′-Biotin-AGGGA TCCTC TAGAC TCTTC T-Cy5–3′; Integrated DNA Technologies). The P18 loop was mutated (mutated part shown in blue) to allow hybridization of its complementary DNA oligo, L18-Cy3 (sequence: 5′-Cy3-ACCAA GAGCG TTATT AAT-3′; Integrated DNA Technologies).

The mutated RNA was stored at −80°C in water at high concentration. Right before hybridization, 4 μM RNA was heated at 90°C in 20 mM Tris (pH 8.0) for 2 min to remove any misfolded secondary structure that could have resulted from the freezing and thawing processes. It was allowed to cool for ≈3 min at room temperature. It was then heated at 37°C for 5 min in 20 mM Tris/50 mM NaCl to allow formation of correctly folded secondary structure. Then the two DNA oligos were added in the same molar ratio as the RNA. The mixture was heated at 37°C for 30 min to allow hybridization of the DNA oligos to the RNA. This sample was stored at 4°C and used for single-molecule FRET measurements for no more than 1 week.

To immobilize RNA in the flow chamber, 0.2 mg/ml Streptavidin (Invitrogen) in buffer A (20 mM Tris/50 mM NaCl) was flowed into the chamber. After 10 min of incubation, the chamber was washed with buffer A. A diluted RNA sample in buffer B (20 mM Tris/1 mM [Mg^{2+}]) was flowed into the chamber. The dilution factor of the RNA sample was adjusted to allow good coverage of RNA molecule for single-molecule measurements; usually 10,000–50,000 dilution was used. After 1–2 min of incubation, the chamber was washed with buffer B and was ready for the [Mg^{2+}]-jump measurement.

Flow Chamber Preparation. An ≈800-μm-wide straight detection channel and two short input channels were cut into an adhesive spacer (Grace Biolabs) (4). A flow chamber was formed by coupling a polyethylene glycol (PEG)-coated coverslip and a glass slide with the adhesive spacer, and holes were drilled through the glass slide to allow buffer change. A layer of poly(dimethylsiloxane) (5) was covalently attached to the top of the slide to help secure the tubing. Epoxy was used to seal the side of the chamber.

Each of the two input channels was connected to a syringe filled with imaging buffer (20 mM Tris with 0.8 mg/ml glucose oxidase, 0.03 mg/ml catalase, 1% 2-mercaptoethanol, and 0.4% glucose) and the desired [Mg^{2+}] (6). Two PHD2000 syringe pumps (Harvard Apparatus) were used to separately control the flow-in speed of the two buffers. The pumps were computer-controlled with a home-developed LabVIEW program. Different flow profiles can be achieved by controlling the two pumps. The flow profile used in this experiment is shown in Fig. 1*A*; the [Mg^{2+}] in the flow chamber alternated between two concentrations with same length of time for the high and low [Mg^{2+}] steps. For the experiments reported in this article, 10 sec was used as the step length.

The preparation of the PEG surface was similar to the published procedure (4). The coverslip was first cleaned by incubating in Piranha solution for 30 min. It was washed with filtered water and then acetone. After allowing the coverslip to sit in acetone (<0.4% H_2O content) for at least 5 min, VECTABOND (Vector Laboratories) was added to the solution at 2% volume ratio. After 5-min incubation, the coverslip was washed with filtered water and dried under nitrogen gas. A PEG solution was made with 100 mg of mPEG (Nektar Therapeutics; MW = 5,000) and 1 mg of biotin-PEG-NHS (Nektar Therapeutics; MW = 3,400) in 1 ml of $NaHCO_3$ (0.1 M, pH 8.2). 50 μl of PEG solution was sandwiched between two VECTABOND-treated coverslips. After a 3-hr incubation, the coverslips were washed with filtered water, dried under nitrogen gas, and stored under vacuum.

Microscope Setup. A home-built objective-type total internal reflection fluorescence (TIRF) microscope was used for the measurement; details of the setup have been reported before (7). A 532-nm diode laser was used to excite Cy3. The emission from Cy3 and Cy5 was separated by dichroic and bandpass filters (Chroma Technology) mounted in a commercial dual channel imaging system (DualView; Optical Insights). The donor (Cy3) and acceptor (Cy5) fluorescence was detected by an iXon DV887-BI CCD (Andor Technology) at a frame rate of 20 frames/sec. The illumination intensity was adjusted with neutral density filters for good S/N and long trajectories before photobleaching. The images were processed with programs written in MATLAB to extract the time trajectories of donor and acceptor molecules for every single RNA molecule. All measurements were conducted at 18–20°C.

Buffer Change Profile Characterization. It takes a finite amount of time for the buffer change to complete. Furthermore, the time and sharpness of the buffer change depend strongly on the lateral position in the channel because of the parabolic flow velocity profile and diffusion (8). To characterize this, one input channel was connected to a fluorescent solution of Rhodamine-6G, and the other one was connected to water. The two inputs were turned on and off alternately as shown in Fig. 1*A*. The fluorescence from Rhodamine-6G was measured with the TIRF setup. Fig. S2 shows the measured buffer change time at several different flow rates near the center lateral position of the flow chamber. The general trend was that the transition time for the buffer change was shorter for higher flow rates. This was expected because the faster the flow rate, the less time for diffusion to mix the two buffers. It can also be seen from Fig. S2 that the transition time starts to plateau at flow rates of ≥50 μl/min. A 50 μl/min flow rate was chosen for all of the experiments, giving an ≈1-sec transition time (Figs. 1*A* and S2) at the center lateral position of the flow chamber.

Cy3 Fluorescence Response to [Mg^{2+}] Change. The ensemble measurement of Cy5 fluorescence shows no dependence on [Mg^{2+}] whereas Cy3 fluorescence was slightly brighter at higher [Mg^{2+}] (data not shown). To study the Cy3 fluorescence dependence on [Mg^{2+}] on the single-molecule level, the Tether-Cy3 oligo (sequence: 5′-Biotin-AGGGA TCCTC TAGAC TCTTC T-Cy3–3′; Integrated DNA Technologies) was immobilized to the PEG surface via streptavidin. The measurement was performed with [Mg^{2+}] alternating between 0.01 and 1 mM and the fluorescence response to the [Mg^{2+}] change was obtained for each single Cy3 dye. Fig. S3 shows example trajectories for single Cy3 molecules in the same field of view. Approximately half of the Cy3 population shows no fluorescence dependence on [Mg^{2+}] whereas the other half instantaneously shows ≈25% fluores-

cence increase when $[Mg^{2+}]$ was increased from 0.01 to 1 mM. This $[Mg^{2+}]$-dependent behavior was also observed for RNA molecules with a fully photobleached Cy5 acceptor. It was often observed in the experiment that when Cy5 was apparently photobleached (i.e., turning into a long dark state), it might still have a significant quenching effect on the donor Cy3 molecule (data not shown) (9). This quenching effect can last as long as tens of seconds before the Cy5 molecule was fully photobleached. This part of the trajectory needs to be excluded from the Cy3 $[Mg^{2+}]$-response analysis.

For the flow rate used, 50 μl/min, it takes a few seconds for the flow front to go through the whole flow channel. Both the time point and the sharpness of the $[Mg^{2+}]$ change depends on the lateral position being measured. No external $[Mg^{2+}]$ reporter was added in the RNA experiments. Instead, the time profile of the buffer change was determined in each local measurement region by recording and averaging the $[Mg^{2+}]$-dependent change of fluorescence brightness of isolated Cy3 molecules (i.e., surface-bound Cy3-DNA oligos not hybridized to RNA, or dual-labeled RNA with a fully photobleached acceptor), which were present in the sample. Fig. 1*A* gives an example of the $[Mg^{2+}]$ response as determined from the brightness change of Cy3 molecules in the RNA $[Mg^{2+}]$-jump experiment. This allows direct, *in situ* determination of the $[Mg^{2+}]$ change profile for the specific region of the channel being imaged.

It was necessary to precisely establish the time interval when $[Mg^{2+}]$ was low or high for analysis of the RNA dynamics in response to the $[Mg^{2+}]$ jump. Each high $[Mg^{2+}]$ interval was defined as starting from the first time point when $[Mg^{2+}]$ starts to increase and ending at the time point right before the $[Mg^{2+}]$ starts to decrease again. Thus, it includes the $[Mg^{2+}]$ increasing shoulder and the period when $[Mg^{2+}]$ was held steadily at high concentration. The low $[Mg^{2+}]$ interval was similarly defined.

As explained in *Discussion*, electrostatic relaxation of RNA structure was always observed upon $[Mg^{2+}]$ change, wherein the E_{FRET} value changes smoothly and follows the $[Mg^{2+}]$-transition curve. This can be used as an alternative indicator of $[Mg^{2+}]$-change time point and allow more flexibility to conduct the $[Mg^{2+}]$-jump experiments.

Choice of E_{FRET} Definition. By the original definition (10, 11), the FRET efficiency was related to the distance between the FRET dye pair as

$$E^*_{FRET} = \frac{I_{D\tilde{A}} - I_{DA}}{I_{D\tilde{A}}} = \frac{1}{1 + R^6/(R^*_0)^6}, \qquad [1]$$

where E^*_{FRET} is the FRET efficiency, $I_{D\tilde{A}}$ and I_{DA} are the photon counts in the donor channel for the single-labeled sample (only labeled with donor) and dual-labeled sample (labeled with both donor and acceptor), respectively, R is the distance between the dye pair, and

$$R^*_0 = (8.79 \times 10^{-5} J q_D n^{-4} \kappa^2)^{1/6} = (C \cdot q_D)^{1/6} \text{ (in Å)}. \qquad [2]$$

In Eq. **2**, J is the overlap of the donor and acceptor spectra, n is the index of refraction of the medium, κ^2 is a geometric factor, and q_D is the quantum yield of the donor. The second equality in Eq. **2** separates the contribution of q_D from other factors.

Quantities I_A and I_D (the photon counts in the acceptor and donor channel for the dual-labeled sample) were more convenient to analyze than I_{DA} and $I_{D\tilde{A}}$. It can be easily seen that the relation between the four quantities is

$$I_{DA} = I_D \text{ and } I_{D\tilde{A}} = I_D + \frac{q_D}{q_A} \cdot I_A. \qquad [3]$$

Using Eqs. **2** and **3**, Eq. **1** can be rewritten as

$$E^*_{FRET} = \frac{\frac{q_D}{q_A} \cdot I_A}{I_D + \frac{q_D}{q_A} \cdot I_A} = \frac{1}{1 + R^6/(C \cdot q_D)}. \qquad [1']$$

A slightly modified definition of the FRET efficiency, $E_{FRET} = I_A/(I_D + I_A)$, is widely applied in experiments to save the effort of measuring q_D and q_A. From Eq. **1′**, the expression for E_{FRET} becomes

$$E_{FRET} = \frac{I_A}{I_D + I_A} = \frac{1}{1 + \frac{q_D}{q_A} \cdot R^6/(R^*_0)^6}$$

$$= \frac{1}{1 + \frac{q_D}{q_A} \cdot R^6/(C \cdot q_D)} = \frac{1}{1 + R^6/(C \cdot q_A)}. \qquad [4]$$

The $[Mg^{2+}]$ dependence of Cy3 fluorescence brightness was assumed to be solely due to the quantum yield change of Cy3 at different $[Mg^{2+}]$. It can be seen from Eq. **1′** that when the distance between the FRET pair is constant, the measured E^*_{FRET} values for the same RNA conformational state will be different at different $[Mg^{2+}]$ because of the quantum yield change of Cy3. However, the quantity E_{FRET} has no dependence on Cy3 quantum yield (Eq. **4**), and the change in the E_{FRET} value can be solely attributed to the distance change between the FRET dye pair (i.e., the conformational change of the RNA molecule). Thus, the definition of FRET efficiency shown in Eq. **4** was adopted for the current $[Mg^{2+}]$-jump experiments.

Determination of E_{FRET} Population Evolution. Figs. 2*C* and 3*C* were generated to quantify the E_{FRET} population evolution over time. For each $[Mg^{2+}]$-jump condition, all of the single-molecule trajectories in one field of view (≈100 RNA molecules) were included in the calculation.

First, the segments of each E_{FRET} trajectory were separated into the low or high $[Mg^{2+}]$ intervals. For each $[Mg^{2+}]$ interval, each segment was further classified into one of two categories depending on whether the RNA molecule was in high or low E_{FRET} state before the $[Mg^{2+}]$ jump. For each category, the E_{FRET} values were histogrammed together, as shown in Figs. 2*B* and 3*B*. For each E_{FRET} histogram, a minimum number of Gaussian functions were chosen to have a good fit of the histogram. The Gaussian fit identifies the number of E_{FRET} levels, the average E_{FRET} values, and the width of the distribution of each E_{FRET} level.

Second, for each category, an E_{FRET} histogram was built at each time point (instead of for the whole $[Mg^{2+}]$ interval as in the first step) and fit with Gaussian functions. The number of Gaussian functions, the average E_{FRET} values, and the width of the distribution of each E_{FRET} level were all taken from the first step and used as known parameters. Only the height of each Gaussian function, which represents the population in each E_{FRET} level, was used as a fitting variable. Figs. 2*C* and 3*C* were plotted by normalizing the total RNA population of each category at each time point to unity.

Determination of Rate Constants. The data of Figs. 2*C* and 3*C* were fit with exponential functions to determine the rate constants of each kinetic step. The RNA conformational change during the ≈1-sec $[Mg^{2+}]$-transition period at the beginning of each curve cannot be well studied because of the inadequate time resolution of the experiment and the different $[Mg^{2+}]$ profile at different positions in the flow chamber. Thus, all of the exponential fits

were done with the later part of the data (i.e., after ≈1 sec) where the [Mg^{2+}] was stable.

For sequential unimolecular reactions, $X_0 \leftrightarrow X_1 \leftrightarrow \cdots \leftrightarrow X_n$, the time evolution of each X_i has the general form

$$X_i = C_i + \sum_{j=1}^{n} A_{ij} e^{-\lambda_j t} \text{ for } i = 1, 2, \ldots, n,$$

where n is the number of independent reaction steps and λ_j are functions of the forward and backward reaction constants of all reaction steps (12).

Fig. 2*C* has only two E_{FRET} states. Fig. 2*C3* shows no detectable dynamics between the two E_{FRET} states as explained in the figure legend. For Fig. 2 *C1*, *C2*, and *C4*, the two curves in each figure were fit simultaneously with exponential functions. All figures can be fit by single exponentials and do not require fitting with bi-exponentials, suggesting that no interconversion of the hidden DOF was observed during the 10-sec [Mg^{2+}] steps. Thus, they can be represented by the simple scheme I ↔ IV. The results were in the following format:

$$[i] = C_i + A_i \cdot e^{-(k_b + k_f) \cdot t} \text{ for } i = \text{I, IV}.$$

The detailed balance relation $C_I \times k_f = C_{IV} \cdot k_b$, which is appropriate for the steady state at the end of each 10-sec interval, allows determination of k_f and k_b from their sum.

Figs. 3 *C1* and *C2* both exhibit four E_{FRET} states and can be explained by the simple linear scheme I ↔ II ↔ III ↔ IV. In Fig. 3*C2*, the time scales were well separated. The transitions between states I and II were very fast. The observed kinetics were complete by the ≈1-sec [Mg^{2+}] transition and were well separated in time from later kinetic steps. The transition between states III and IV was very slow, and no detectable transition was observed during the 10-sec [Mg^{2+}] step. Thus, only the transition between states II and III was considered, and it was determined to be analogous to Fig. 2*C*.

In Fig. 3*C1*, the simultaneous fitting of all of the curves require fitting with bi-exponential functions. This suggests that only the contributions of two independent kinetic steps were observed within the 10-sec [Mg^{2+}] step. It can be seen from the figure that the kinetics of state IV was the least well observed. Thus, only the kinetics between state I, II, and III was considered. In this case, the fit functions were in the following format:

$$[i] = C_i + A_i \cdot e^{-\lambda_1 \cdot t} + B_i \cdot e^{-\lambda_2 \cdot t} \text{ for } i = \text{I, II, III}$$

where

$$\lambda_{1,2} = \frac{a_{11} + a_{22}}{2} \cdot \left(1 \pm \sqrt{1 - 4 \cdot \frac{a_{11} \cdot a_{22} - a_{12} \cdot a_{21}}{(a_{11} + a_{22})^2}}\right).$$

with $a_{11} = k_{f(I,\,II)} + k_{b(I,\,II)} + k_{f(II,\,III)}$; $a_{12} = k_{f(I,\,II)} - k_{b(II,\,III)}$; $a_{21} = -k_{b(II,\,III)}$; and $a_{22} = k_{b(II,\,III)}$ (12).

The detailed balance relations between states at steady state, $C_I \cdot k_{f(I,\,II)} = C_{II} \cdot k_{b(I,\,II)}$ and $C_{II} \cdot k_{f(II,\,III)} = C_{III} \cdot k_{b(II,\,III)}$, were again used for determination of each k_f and k_b. There were two solutions from the above equations, with the difference of either I ↔ II or II ↔ III being the faster process. It was clear from Fig. 3*C1* that I ↔ II was faster than II ↔ III; thus, the other solution was ruled out.

The resulting rate constants are summarized in Table S1. The error of the rate constants was estimated by recalculating the rate constants with all fit parameters set at one standard error away from the curve fitting results (the standard error of each fit parameter was taken directly from the output of the curve fitting algorithm). Other factors that might contribute to the errors were not taken into consideration at this stage.

Contrasting with Equilibrium Measurements. The periodic perturbation approach should be understood to be a complementary method to more traditional single-molecule equilibrium measurements. As stated in the main text, as the period of the perturbation becomes long compared with the relaxation times (dynamics) under investigation, then the system will reach equilibrium at the end of each interval (e.g., folding at high Mg^{2+} or unfolding at low Mg^{2+}). The associated distribution of first passage times could be analyzed by a fluctuation dissipation theorem (FDT), assuming linear response for perturbation not too far from equilibrium. Of course, this provides a direct connection with measurements of equilibrium fluctuations and distributions of dwell times. As we have pointed out in the main text, the system does not achieve equilibrium if the perturbation intervals are shorter than the slowest relaxation times. The first passage times, and associated kinetic decays, will differ from those expected from FDT for Markovian dynamics. We have shown elsewhere (unpublished observations) that the dynamics observed in Figs. 2 and 5 can be captured with a generalized Langevin equation treatment, with appropriate memory kernels, and necessarily non-Markovian dynamics. Furthermore, time correlation function analysis of the datasets reported in the present article show that the correlation functions were not time-stationary in the high [Mg^{2+}] intervals posing a challenge for analytical analysis (unpublished observations).

It should be said that there were limits to the periodic perturbation method. Information about dynamics were necessarily focused into the time duration of each perturbation interval whereas equilibrium single-molecule trajectories were typically (ideally) of long intervals and have decades of temporal dynamic range. Conversely, equilibrium experiments generally rarely sample conformations near the transition states associated with conformational change whereas the periodic perturbation experiment tends to cause the molecules in the resultant non-equilibrium steady state(s) to sample conformational space that can be chosen to be closer to these transition state regions. Further experiments, numerical analysis, and simulations are required to understand to what extent one can control the phase space sampled.

Additional Comments on Cooperative RNA Folding. The relaxation kinetics of state II were particularly interesting. State II was the first well populated intermediate on the folding pathway when [Mg^{2+}] was increased from 0.01 mM to 0.4 mM or 1.0 mM; thus, it probably involves some tertiary interactions that were stabilized at [Mg^{2+}] ≥ 0.4 mM. Equilibrium measurements (Fig. 3*B Insets*) (13) show that state II was only slightly populated at [Mg^{2+}] = 0.4 mM, and its E_{FRET} value was indistinguishable from the native state at [Mg^{2+}] = 1.0 mM. If state II was sampling the transition state region, then any tertiary interactions formed in state II early on the folding pathway may be part of the cooperative folding interactions of CthermoL18 at high [Mg^{2+}] (1). At [Mg^{2+}] = 1.0 mM, when other cooperative folding structural elements were also stable, the stability of all interactions were cooperatively enhanced (14) and the RNA molecule was "locked" in the native state. At [Mg^{2+}] = 0.4 mM, the other tertiary interactions were not in place with high probability, and state II was thus not stable enough to be significantly populated under equilibrium conditions; it was a local but not a global minimum on the folding pathway.

1. Fang XW, *et al.* (2001) The thermodynamic origin of the stability of a thermophilic ribozyme. *Proc Natl Acad Sci USA* 98:4355–4360.

2. Smith GJ, Sosnick TR, Scherer NF, Pan T (2005) Efficient fluorescence labeling of a large RNA through oligonucleotide hybridization. *RNA* 11:234–239.

3. Dorywalska M, *et al.* (2005) Site-specific labeling of the ribosome for single-molecule spectroscopy. *Nucleic Acids Res* 33:182–189.
4. van Oijen AM, *et al.* (2003) Single-molecule kinetics of lambda exonuclease reveal base dependence and dynamic disorder. *Science* 301:1235–1238.
5. Song H, Ismagilov RF (2003) Millisecond kinetics on a microfluidic chip using nanoliters of reagents. *J Am Chem Soc* 125:14613–14619.
6. Yildiz A, *et al.* (2003) Myosin v walks hand-over-hand: Single fluorophore imaging with 1.5-nm localization. *Science* 300:2061–2065.
7. Qu XH, Wu D, Mets L, Scherer NF (2004) Nanometer-localized multiple single-molecule fluorescence microscopy. *Proc Natl Acad Sci USA* 101:11298–11303.
8. Kamholz AE, Yager P (2001) Theoretical analysis of molecular diffusion in pressure-driven laminar flow in microfluidic channels. *Biophys J* 80:155–160.
9. Huang ZX, *et al.* (2006) Spectral identification of specific photophysics of cy5 by means of ensemble and single molecule measurements. *J Phys Chem A* 110:45–50.
10. Förster T (1965) Delocalized excitation and excitation transfer. *Modern Quantum Chemistry, Istanbul Lectures, Part III: Action of Light and Organic Crystals*, ed Sinanoglu O (Academic, New York), pp 93–137.
11. Selvin PR (1995) Fluorescence resonance energy transfer. *Methods Enzymol* 246:300–334.
12. Cantor CR, Schimmel PR (1980) *The Behavior of Biological Macromolecules* (Freeman, San Francisco).
13. Smith G, *et al.* (2008) A large collapsed-state RNA can exhibit simple exponential single-molecule dynamics. *J Mol Biol*, in press.
14. Fang XW, Srividya N, Golden BL, Sosnick TR, Pan T (2003) Stepwise conversion of a mesophilic to a thermophilic ribozyme. *J Mol Biol* 330:177–183.

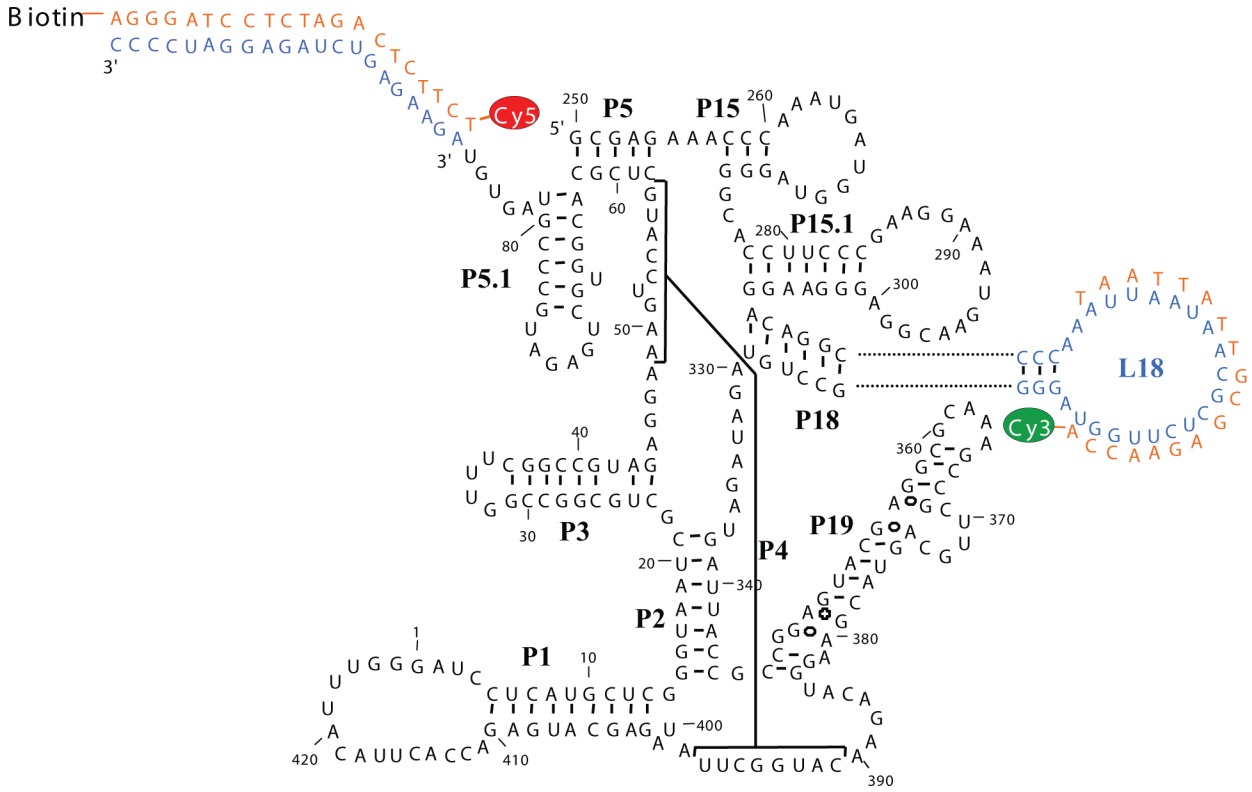

Fig. S1. The secondary structure of CthermoL18 RNA. The original sequence of wild-type Cthermo RNA molecule is shown in black. The mutated part of the RNA sequence for attaching FRET dyes and biotin are shown in blue. The DNA oligos with FRET fluorophores and biotin at the end are shown in orange. The hybridization of the DNA oligos in orange to the mutated RNA sequences in blue allows attachment of FRET dyes to the RNA and the attachment of biotin for immobilizing the RNA molecule to surface.

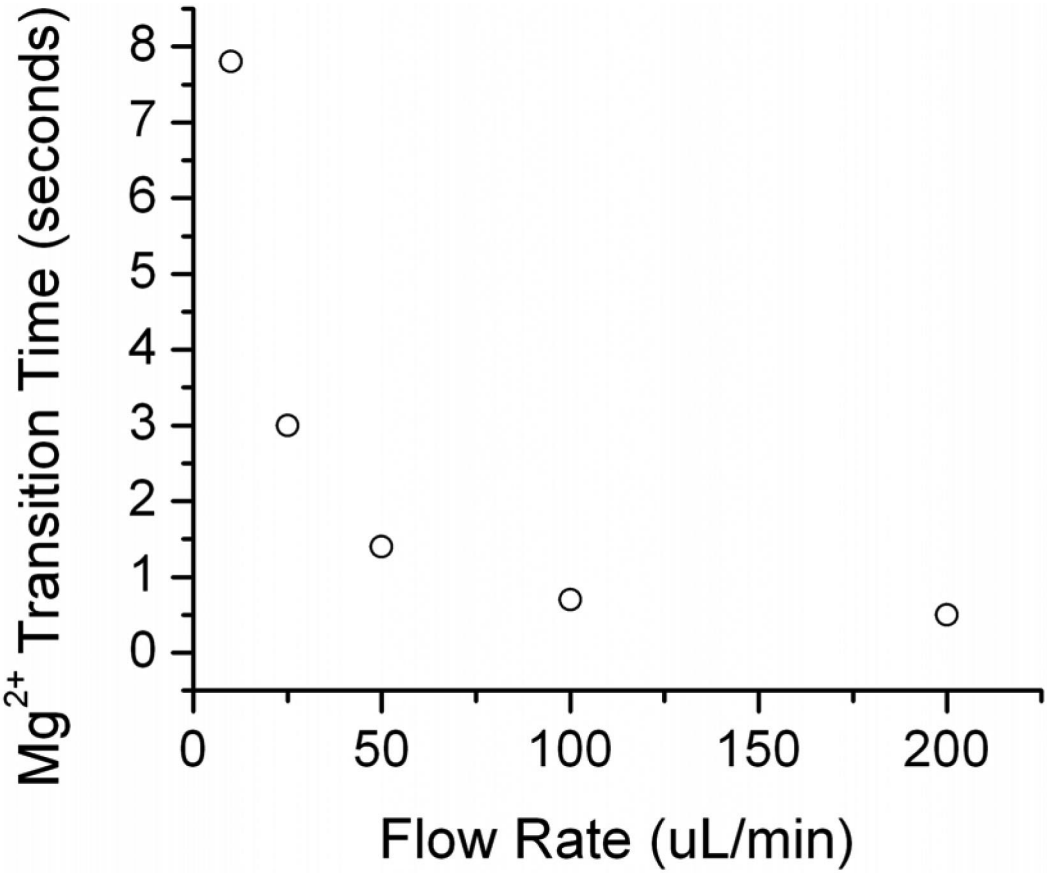

Fig. S2. [Mg^{2+}]-transition time vs. flow rate near the center lateral position of the flow chamber. The result was obtained by alternating between fluorescent solution and water (see *Buffer Change Profile Characterization* in *SI Materials and Methods* for more details). 50 μl/min was chosen for the RNA experiments in this article, which gives an $\approx$1-sec buffer change time near the center lateral position of the flow chamber.

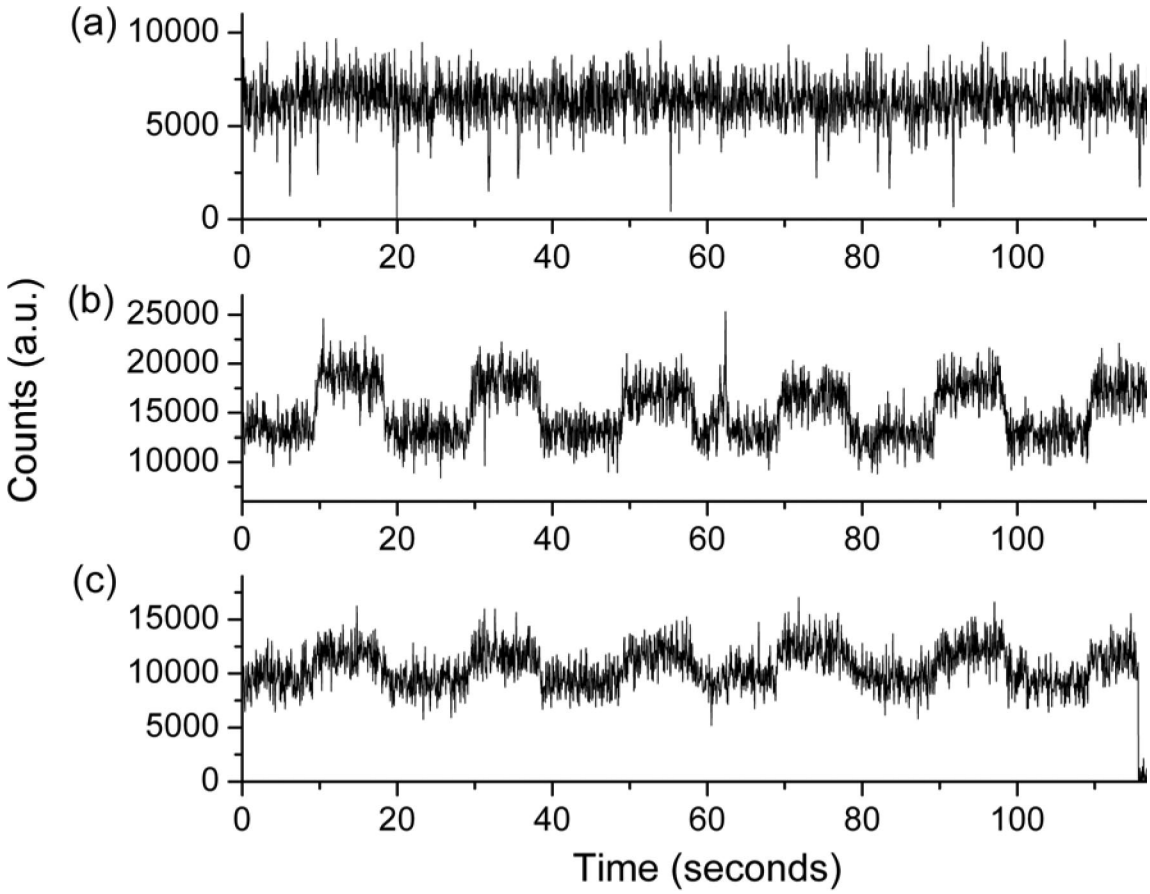

Fig. S3. Example trajectories of the fluorescence brightness dependence on [Mg^{2+}] for three single Cy3 molecules in the same field of view when [Mg^{2+}] alternates between 0.01 and 1 mM. (*a*) An example for Cy3 molecules that have no detectable response to [Mg^{2+}] change. (*b* and *c*) Examples for Cy3 molecules that show ≈25% increase in brightness when [Mg^{2+}] was changed from 0.01 to 1 mM. The Cy3 molecule in *c* photobleached at the end where the count dropped to 0. It can be seen that the fluorescence change in the two trajectories were synchronized in time. This suggests that the Cy3 [Mg^{2+}]-dependent fluorescence response was almost instantaneous in time, and there was no high free energy barrier crossing involved in this process that will cause a response time difference from molecule to molecule. The two subpopulations ([Mg^{2+}]-sensitive and -insensitive) occupy ≈50% of the whole population each and both were easily observed in one field of view.

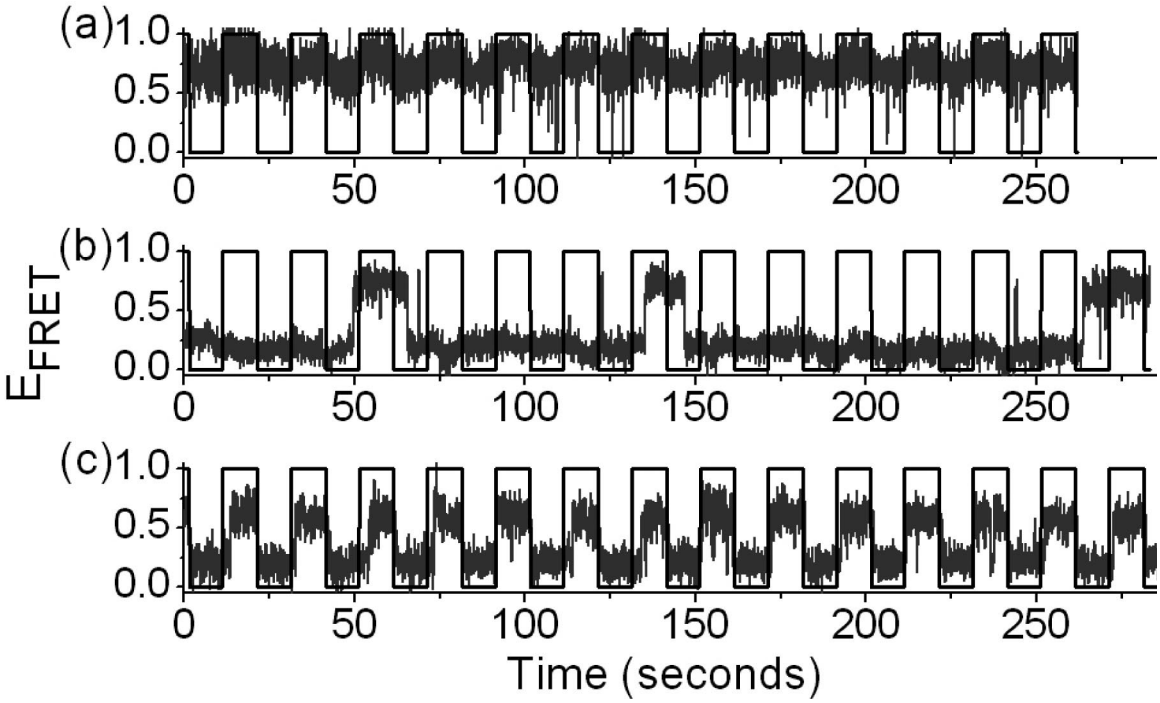

Fig. S4. Example trajectories showing the long memory in the observed dynamics due to the slow dynamics of the hidden DOF. The [Mg^{2+}] was alternated between 0.01 and 0.1 mM. The trajectories were from three RNA molecules in the same field of view. (*a*) The RNA molecule essentially stayed in the high E_{FRET} state. (*b*) The RNA molecule stayed primarily in the low E_{FRET} state. (*c*) The RNA molecule went obediently back and forth between the low and high E_{FRET} states closely following the [Mg^{2+}] change. The difference in the dynamics was due to the difference in the ''hidden'' part of the RNA structure that does not reflect in the observed E_{FRET} values but can affect the observed dynamics of the FRET axis. The lengths of all three trajectories were limited by the photobleaching of the fluorophores.

Table S1. Summary of time constants for the exponential fit to the E_{FRET} evolution in Figs. 2*C* and 3*C*

[Mg^{2+}]-jump conditions				k_f, s^{-1}	k_b, s^{-1}
0.01 ↔ 0.1 mM	Low [Mg^{2+}] interval	Starting from low E_{FRET} state	I ↔ IV	0.24 ± 0.02	0.41 ± 0.03
		Starting from high E_{FRET} state	IV ↔ I	0.23 ± 0.02	0.27 ± 0.02
	High [Mg^{2+}] interval	Starting from low E_{FRET} state	I ↔ IV	0.11 ± 0.01	0.26 ± 0.02
		Starting from high E_{FRET} state	IV ↔ I	Very slow	—
0.01 ↔ 0.4 mM	High [Mg^{2+}] interval	Starting from low E_{FRET} state	I ↔ II	0.8 ± 0.2	0.9 ± 0.2
			II ↔ III	0.29 ± 0.08	0.10 ± 0.03
			III ↔ IV	Slow	—
0.01 ↔ 1.0 mM	High [Mg^{2+}] interval	Starting from low E_{FRET} state	I ↔ II	Very fast	Slow
			II ↔ III	0.22 ± 0.02	0.18 ± 0.02
			III ↔ IV	Very slow	—

For the transition X ↔ Y, k_f is for X → Y and k_b is for Y → X.

— represents rate constants that cannot be determined from the current [Mg^{2+}]-jump experiments. See *Determination of Rate Constants* in *SI Materials and Methods* for details of determination of the rate constants and errors.